Composites Science and Technology 268 (2025) 111213

Contents lists available at ScienceDirect

Composites Science and Technology

journal homepage: www.elsevier.com/locate/compscitech

Self-healing of polyamide 6/cyclic olefin copolymer/carbon fiber composites under quasi-static, impact, and fatigue conditions

M. Coser [a,b,1], D. Perin [a,b,*,1], G. Fredi [a,b,**], L. Aliotta [b,c], V. Gigante [b,c], A. Lazzeri [b,c], A. Dorigato [a,b], A. Pegoretti [a,b]

[a] Department of Industrial Engineering, University of Trento, Via Sommarive 9, 38123, Trento, Italy
[b] Interuniversity National Consortium of Materials Science and Technology, Via Giusti 9, 50121, Florence, Italy
[c] University of Pisa, Department of Civil and Industrial Engineering, Via Diotisalvi, 2, 56122, Pisa, Italy

ARTICLE INFO

Keywords:
Self-healing
Thermoplastic composites
Injection molding
Fatigue
Fracture surface

ABSTRACT

This study investigates the self-healing capabilities of polyamide 6 (PA6) composites containing a cyclic olefin copolymer (COC) as a healing agent and a discontinuous carbon fiber (CF) reinforcement under quasi-static, impact, and fatigue loading conditions. To this aim, PA6/COC (30 wt%)/CF (20 wt%) composites were prepared via melt-compounding and injection molding. The microstructure, mechanical properties, and self-healing behavior of the composites with COC were compared with those of the reference PA6/CF (20 wt%). Although the addition of COC slightly reduces the quasi-static mechanical properties, it significantly improves the impact resistance. The presence of COC domains allow healing efficiencies (HE) of up to 80 % in impact tests, whereas lower HE values are found in quasi-static fracture tests owing to matrix plasticization hindering the COC flow in the fracture zone. Notably, fatigue testing reveals the ability of PA6/COC/CF composites to repair microdamage during thermal mending, extending their own fatigue life by 77 %, while virgin samples are not able to heal. These results highlight the potential of intrinsic self-healing thermoplastic composites to extend the service life of structural composites, particularly under cyclic loading conditions.

1. Introduction

Self-healing composites represent a transformative approach to address the most significant challenges in composite material design, that is, damage tolerance and longevity [1,2]. By incorporating mechanisms that can autonomously repair microdamage, these advanced materials can extend the service life and reliability of structural components across various engineering applications [3]. Self-healing strategies can be broadly classified into extrinsic and intrinsic types. Extrinsic systems incorporate microcapsules or hollow fibers that release reactive chemicals upon damage to fill cracks and cure or polymerize in situ [4,5]. Intrinsic systems, on the other hand, utilize resources already present in the polymer matrix [6], such as reversible chemical bonds, Diels-Alder reactions, disulfide linkages, or thermoplastic healing agents. This last strategy involves incorporating polymers with low softening (melting or glass transition) temperatures directly into the matrix during manufacturing. When damage occurs, the application of an external stimulus (e.g., heat, voltage, or magnetic field) causes these agents to soften and flow into the damaged areas, effectively repairing the cracks upon cooling. This process can be repeated multiple times and does not require the use of expensive matrices or the inclusion of separate capsules or vascular networks, thus simplifying the manufacturing process and reducing costs [7].

Although the inclusion of thermoplastic healing agents has been extensively studied in thermosetting polymers [8,9], a critical knowledge gap remains in understanding similar phenomena in thermoplastic matrix composites, which can be interesting from an engineering perspective thanks to their recyclability, repairability, and faster manufacturing cycles, which are increasingly important in the context of sustainable material development [10–12]. In recent years, our group has focused on developing and optimizing self-healing thermoplastic matrices based on polyamide 6 (PA6) containing polycaprolactone (PCL) or cyclic olefin copolymer (COC) as healing agents [13,14]. While various thermoplastic healing agents have been explored for self-healing

* Corresponding author. Department of Industrial Engineering, University of Trento, Via Sommarive 9, 38123, Trento, Italy.
** Corresponding author. Department of Industrial Engineering, University of Trento, Via Sommarive 9, 38123, Trento, Italy.
E-mail addresses: davide.perin-1@unitn.it (D. Perin), giulia.fredi@unitn.it (G. Fredi).
[1] These authors contributed equally.

https://doi.org/10.1016/j.compscitech.2025.111213
Received 23 January 2025; Received in revised form 24 March 2025; Accepted 28 April 2025
Available online 28 April 2025

polymer composites, COC offers several distinct advantages over alternatives such as PCL. Our previous work [13,14] demonstrated that COC provides superior thermal stability and better chemical compatibility with PA6. This was likely at the basis of the superior mechanical properties retention after healing with COC, with K_{IC} retention reaching approximately 80 % in impact mode for COC-based systems versus 53 % for PCL-based counterparts. Finally, our recent work on compatibilization of PA6/COC blends [15] has demonstrated excellent morphology control and the possibility of fine tuning the COC domain size to achieve optimal distribution of the healing agent in the matrix. In particular, the PA6/COC system with 30 wt% COC showed the most promising results. The addition of compatibilizers such as ethylene glycidyl methacrylate (E-GMA) further increased the mechanical and self-healing properties of the blend by ensuring fine microstructure, homogeneous COC distribution, and adequate interfacial bonding.

The evaluation of self-healing capabilities requires careful consideration of damage mechanisms across different scales [16]. Macroscopic damage assessment using traditional bending, fracture mechanics, compression after impact, or impact tests often results in catastrophic failure with reinforcement rupture. However, such damage cannot be healed via a self-healing matrix, and the properties of the healed composite cannot match those of the virgin one. In other words, intervening with a thermal mending action on a composite with damaged reinforcement is not an effective way to exploit the self-healing capabilities of the matrix, and may not even be a reasonable way to test the healing efficiency. Instead, fatigue testing offers a more sophisticated approach for understanding material repairability. This method enables the controlled insertion of microdamage, allowing researchers to investigate healing mechanisms without compromising the structural integrity of the reinforcements. Fatigue testing uniquely simulates real-world loading conditions, providing insights into how small matrix cracks propagate and potentially heal under cyclic stress, which is critical for predicting the long-term performance.

The existing literature on the fatigue resistance of self-healing composite materials has predominantly focused on fatigue testing of extrinsic [17,18] and/or thermosetting systems [19]. For example, Pingkarawat et al. [20–22] and Ladani et al. [23] focused on carbon/-epoxy composites, demonstrating that the introduction of thermoplastic healing agents can retard fatigue crack growth. However, these studies have been limited to thermosets, leaving a significant knowledge gap in understanding the fatigue behavior and self-healing mechanisms of thermoplastic composites. Notably, no comprehensive studies have explored thermal healing of microdamage under fatigue conditions for thermoplastic composite systems, highlighting the need for further research in this area.

Hence, the objective of this study is to characterize the self-healing potential of thermoplastic composites based on PA6/COC reinforced with discontinuous carbon fibers (CFs). Through a systematic investigation of the microstructure, mechanical properties, and healability under quasi-static, impact, and fatigue loading, we aim to evaluate the potential of these materials to extend fatigue life and enhance long-term durability compared with reference PA6/CF composites. This study seeks to provide insights into the mechanisms of damage and healing, ultimately contributing to the sustainable development of advanced composite materials for engineering and industrial applications.

2. Materials and methods

2.1. Materials

The selected matrix was PA6 Radilon S 24E 100 NAT, kindly provided by Radici Group SpA (Gandino, Italy) in pellet form (density = 1.14 g/cm^3, melting temperature = 220 °C). The healing agent was Topas COC 9506F-500 (TOPAS Advanced Polymers GmbH, Raunheim, Germany) delivered in pellet form (glass transition temperature,T_g = 65 °C; norbornene content = 61 wt%; density = 1.01 g/cm^3; MFI 0.9 g/10 min (190 °C; 2.16 kg)). The E-GMA compatibilizer was purchased from Merck KGaA (Darmstadt, Germany) in form of granules characterized by an MFI of 5 g/10 min (190 °C, 2.16 kg) and a glycidyl methacrylate content of 6.5–9.0 wt %. E-GMA was selected as a compatibilizer due to the possibility of a chemical reaction with PA6 and only a partial physical interaction with the COC, as shown in a preliminary study [15]. Thus, the interfacial adhesion can be enhanced without hindering the flow of the healing agent in the crack zone. Discontinuous CFs were kindly supplied by Zoltek Corporation (Bridgeton, MO, US). The selected chopped CFs were Panex PX35 type-95, with a polyamide-compatible sizing content of 2.75 wt%, average length of 6 mm, and average diameter of 7.2 μm, as specified in the product datasheet.

2.2. Sample preparation

Preparation of PA6/COC/E-GMA blends. PA6 granules were dried at 80 °C for 12 h in a vacuum oven, whereas the COC and E-GMA pellets were dried at 50 °C in a ventilated oven for 12 h. Initially, PA6 and COC were melt compounded at a PA6/COC weight ratio of 70/30 in a Thermo Haake Rheomix 600 internal mixer equipped with counter-rotating rotors operating at 60 rpm at 230 °C for 1 min. E-GMA (5 wt%) was then added, and the material was mixed for a total processing time of 6 min. The PA6/COC ratio was selected according to a previous study by our group [13], which showed that 30 wt% COC is an optimal amount to achieve self-healing properties, whereas an E-GMA fraction of 5 wt% was detected as the optimal concentration in a subsequent work of our group [24], which highlighted that 5 wt% E-GMA promoted microstructural refinement and further enhanced the self-healing capability. After compounding, the material was pelletized with a Piovan RN166/1 grinder equipped with a 3-mm sieve.

Preparation of the composites. The pellets (of either neat PA6 or PA6/COC/E-GMA blends) were dried using a DP604 PIOVAN dryer (PIOVAN, Venezia, Italy) at 80 °C for 12 h and then inserted into a semi-industrial Comac EBC 25HT (COMAC, Cerro Maggiore, Italy) twin-screw extruder (length/diameter = 44), composed of 11 different temperature-controlled zones with five separate metering zones to ensure uniform melt homogenization and very precise control of the final CF concentration. In particular, the extruder was composed of four distinct feeding zones: the matrix (either neat PA6 or the prepared PA6/COC/E-GMA self-healing blend) was introduced into the main feeder, suitable for granules, while CFs were introduced in a side feeder. A carbon fiber content of 20 wt% was selected according to data reported in the literature and relevant industrial standards for PA6-based carbon fiber composites [25]. The temperature profile applied from the feed to the die was 170/190/220/230/230/230/230/220/210/210/200 °C. The feed rate was set at 3 kg/h, while the screw speed was set to 120 rpm for neat PA6 and the PA6/COC/E-GMA self-healing blend, 110 rpm for PA6 reinforced with 20 wt% CF, and 180 rpm for the PA6/COC/E-GMA reinforced with 20 wt% CF. The extruded filaments were cooled in a water bath at room temperature and pelletized using an automatic cutter. The pellets were then dried in a drier at 80 °C and injection molded using a Megatech H10/18 injection molding machine (Tecnicaduebi, Fabriano, Italy), with a temperature profile of 190/245/255 °C, injection pressure of 70 bar, mold temperature of 90 °C, injection holding time of 3 s, and cooling time of 1 min. The specimens obtained were of type ISO 527-1A dumbbell geometry (overall length = 150 mm,

Table 1
List of prepared blends and composites with nominal weight compositions.

Sample code	PA6 [wt%]	COC [wt%]	E-GMA [wt%]	CF [wt%]
PA6	100.0	–	–	–
PA6CF20	80.0	–	–	20.0
PA6COC	66.5	28.5	5.0	–
PA6COCCF20	53.2	22.8	4.0	20.0

gauge length = 80 mm, width = 10 mm, thickness = 4 mm). Table 1 lists the codes and composition of the prepared samples.

2.3. Characterization

2.3.1. Rheological properties

Dynamic rheological measurements were conducted using an HR-2 Discovery Hybrid Rheometer (TA Instruments, New Castle, DE, USA) operating in a parallel-plate configuration (plate diameter = 25 mm, gap = 1 mm). Frequency sweep tests were performed at 230 °C in air, in a frequency range from 0.05 to 600 rad/s, under a strain amplitude of 1 %. Through these tests, it was possible to determine the trends of the complex viscosity (η^*), storage modulus (G'), and loss modulus (G'') as functions of frequency. A minimum of three specimens were tested for each composition.

2.3.2. Microstructural properties and density

Light optical microscopy was performed on the polished surfaces of the as-produced samples. The samples were embedded in an epoxy resin and cured for 24 h at room temperature. After curing, the samples were removed from the mold and polished using a Struers LaboPol-5 system operating at 250 rpm. The first polishing step was performed using sequential silicon carbide abrasive papers with grit polishing sizes of 240, 800, 1200, and 4000, while the second step was carried out using polishing cloths of 3 μm and 1 μm. The tests were performed using a CH 9435 Heerbrugg optical microscope (Heerbrugg, Switzerland). ImageJ® software (National Institutes of Health campus, Bethesda, USA, release 1.8) was used to measure the diameter of the COC domains and fiber length distribution.

Field emission scanning electron microscopy (FESEM) was performed on the cryo-fractured surfaces using a Zeiss Supra 40 microscope operating at an acceleration voltage of 2.5 kV. A Pt/Pd (80:20) conductive coating was sputtered onto the specimens before observation to render them electrically conductive.

The density (ρ_{exp}) was measured with a pycnometer Micrometrics AccuPyc 1330. The volume fraction of voids (V_v) in the composites was then calculated using Equation (1),

$$V_v = \frac{\rho_{th} - \rho_{exp}}{\rho_{th}} \cdot 100 \tag{1}$$

where the theoretical densities (ρ_{th}) were calculated via Equation (2)

$$\rho_{th} = \frac{1}{\frac{w_{f,exp}}{\rho_f} + \frac{1-w_{f,exp}}{\rho_m}} \tag{2}$$

where $w_{f,exp}$ is the experimental fiber weight fraction measured via thermogravimetric analysis (TGA) and ρ_f and ρ_m are the experimental density values of the matrix (PA6 or PA6COC).

2.3.3. Thermal properties

Differential scanning calorimetry (DSC) tests were performed using a Mettler DSC30 instrument under a nitrogen flow of 100 ml/min, from −20 °C to 250 °C, with a heating/cooling rate of 10 °C/min. Each specimen was subjected to a first heating scan, a cooling scan, and a second heating scan. From the obtained thermograms, the thermal transitions of the constituents of the blends were measured, i.e., the T_g of COC and the melting/crystallization temperatures and enthalpy values of PA6 (T_m, ΔH_m, T_c, and ΔH_c). The degree of crystallinity (χ) of the PA6 phase in the blends was evaluated via Equation (3),

$$\chi = \frac{\Delta H_m - \Delta H_{cc}}{\Delta H_m^* \cdot \omega_{PA6}} \cdot 100 \tag{3}$$

where ΔH_{cc} is the enthalpy of cold crystallization of PA6, ΔH_m^* is the melting enthalpy of fully crystalline PA6 (230 J/g [26]), and ω_{PA6} is the weight fraction of PA6 in the blend.

Thermogravimetric analysis (TGA) was performed on the prepared blends and composites to assess how the resistance to thermal degradation varied when the healing agents or reinforcements were added. Tests were performed using a TA Instruments Q5000 IR thermobalance at a heating rate of 10 °C/min up to 700 °C under a nitrogen flow of 10 ml/min, on specimens of approx. 10 mg. The TGA tests allowed the calculation of the temperature associated with a mass loss of 1 %, 3 % and 5 % ($T_{1\%}, T_{1\%}, T_{5\%}$) and the temperature associated with the maximum mass loss rate (T_D), considered as the peak of the mass loss derivative (DTG) curve.

An additional test was performed on the CF-reinforced composites to recover the carbon fibers and measure the effective fiber length. Specimens of approx. 10 mg were heated at 10 °C/min to 500 °C, followed by an isothermal step at 500 °C for 5 min. This treatment led to the complete degradation of the matrix while leaving the fibers intact. A similar approach was used by Karsli et al. [27] to measure the CF length in PA6/CF composites. The obtained fibers were dispersed in acetone (98.5 %), deposited on a Petri dish, and observed using a light microscope Zeiss AX10 with a 10x objective lens. The resulting images were analyzed using ImageJ software to obtain the length distribution.

2.3.4. Mechanical properties

Quasi-static tensile tests were performed at ambient temperature using an Instron® 5969 tensile testing machine (ITW Test & Measurement and Equipment, USA) equipped with a 10 kN load cell, testing ISO 527 1A specimens. The tests were performed at a crosshead speed of 5 mm/min and at least 12 specimens were tested for each composition. These tests were performed to determine the ultimate tensile stress (σ_{UTS}) and the strain at break (ε_b). For the evaluation of the elastic modulus (E), additional tests were carried out using the same machine equipped with an Instron® 2620-601 extensometer, at a crosshead speed of 1 mm/min. The elastic modulus was calculated as the secant modulus between strain values of 0.05 % and 0.25 % for at least five specimens per sample.

The fracture toughness was tested on single-edge notched bending (SENB) specimens with dimensions of 44 × 10 × 5 mm^3, a sharp notch 5 mm in depth, and a span length of 40 mm. The specimens were obtained from the central portion of injection-molded 1A dumbbell specimens. Tests in the quasi-static mode were performed according to ASTM D5045 using an Instron® 5969 machine. Three-point bending tests on notched specimens were performed at a crosshead speed of 10 mm/min, and at least 12 specimens for each composition were tested. From the load-displacement curves, the maximum load (P_{max}) was determined, and the critical stress intensity factor (K_{IC}) was calculated via Equation (4),

$$K_{IC} = \frac{P_{MAX}}{BW^{1/2}} \cdot f(x), \tag{4}$$

where B is the thickness of the specimen, W is its width, and $f(x)$ is a calibration factor defined by the ASTM D5045 standard, being $x = a/W$ the ratio between the notch depth (a) and the specimen width. From the integration of the load-displacement curves and the evaluation of the system compliance, the critical strain energy release rate (G_{IC}) values were calculated via Equation (5),

$$G_{IC} = \frac{\Delta U}{BW\varphi}, \tag{5}$$

where ΔU is the difference between the total energy absorbed by the specimens and the energy absorbed in the indentation tests, and φ is the energy calibration factor calculated as reported in ASTM D5045.

Charpy impact tests were performed following the ISO 179 standard using a CEAST 6549 Charpy pendulum equipped with a hammer ISO 5 J M1257 at an impact speed of 1 m/s. This low speed was chosen to reduce the inertial peaks in the force-displacement signal. A thin plasticine layer was used to dampen the vibrations and further reduce the inertial

peaks. The test was conducted on rectangular specimens obtained from the central portion of injection-molded 1A dumbbell specimens with nominal dimensions of 80 × 10 × 4 mm^3, notch depth of 2 mm, and notch tip radius of 0.25 mm. A span length of 62 mm was used, and at least ten specimens were tested for each sample. The test allowed the measurement of the maximum load reached during the tests (F_{max}), specific energy absorbed at the maximum load ($E_{sp,max}$), and specific energy absorbed at break ($E_{sp,tot}$). The tested samples were analyzed under a light microscope to measure the effective cross-section and observe the morphology of the fracture surfaces.

Fatigue tests were conducted on CF-reinforced composites in tension-tension mode on the as-produced 1A samples. Tests were performed at 20 °C with a Walter + Bai Axial/Torsional Universal Testing Machine Type LFV 25 kN - T75 Nm (Löhningen, Switzerland), under a sinusoidal load at a frequency of 3 Hz, speed of 0.1 kN/s, and a load ratio (R) of 0.1. Before starting the test, the force was increased linearly up to the mean load, and the specimens were then subjected to an alternating cycle. The clamps were manually closed using a torque wrench of 25 N m. A frequency of 3 Hz was selected to avoid overheating of the specimens. Preliminary tests were performed on PA6CF20 samples at 0.6• σ_{UTS}, R = 0.1, and 5 Hz, and overheating of the specimen occurred, as measured with an infrared thermal camera FLIR E6 (FLIR Systems Srl (Limbiate, Italy, emissivity 0.85), thus causing a decrease in the mechanical properties. Hence, the frequency was lowered to 3 Hz and no overheating was detected. Fatigue testing was performed at load levels of 0.9• F_m, 0.8• F_m, 0.7• F_m, 0.6• F_m, and 0.5• F_m, where F_m is the average σ_{UTS} multiplied by the cross-sectional area of the specimens. The results of the test were used to build the Wöhler curves (S–N curves), i.e., a graphical representation of the relationship between the maximum applied stress and the number of cycles to failure.

2.3.5. Evaluation of the healability of the prepared samples

The healability was evaluated by comparing the mechanical performance of the as-prepared composites ("virgin" materials) with those of damaged and then thermally mended samples ("healed" materials). In the literature, the efficacy of the healing process is commonly described in terms of healing efficiency (*HE*) [28], typically expressed as the ratio of the strength, stiffness, or toughness of the material after healing to that of the virgin material. In this work, thermal mending was performed on the prepared samples both after macrodamage was produced via fracture toughness and Charpy impact tests, and after microdamage was produced via fatigue tests. Although healing after macrodamage has been extensively documented in the literature, thermal mending of samples subjected to a certain amount of fatigue damage, but not yet catastrophically failed, remains less studied. In this study, we considered and compared both approaches.

For macrodamaged samples, all the specimens tested in quasi-static fracture toughness and Charpy impact tests were thermally mended in an oven at 160 °C for 60 min under an applied pressure of 0.5 MPa applied via a lab-made device (comprehensively described in Refs. [13,14]) to keep the fracture surfaces in close contact. These healing parameters were selected because they were identified as optimal in our previous work [13,24]. The specimens subjected to thermal mending were tested again using quasi-static fracture toughness and Charpy tests. Thus, the respective healing efficiencies, i.e., HE_{KIC} and HE_{Charpy} were evaluated by Equations (6) and (7), respectively,

$$HE_{KIC} = \frac{K_{IC\_healed}}{K_{IC\_Virgin}} \cdot 100 \tag{6}$$

$$HE_{Charpy} = \frac{E_{sp,tot\_healed}}{E_{sp,tot\_virgin}} \cdot 100 \tag{7}$$

where $K_{IC_{Virgin}}$ and K_{IC_healed} are the critical stress intensity factors of the virgin and healed specimens and E_{sp,tot_virgin} and E_{sp,tot_healed} the Charpy impact energy of the virgin and healed specimens, respectively.

To evaluate the healability of microdamaged samples, composite specimens were tested under fatigue conditions with a stress amplitude of 0.67 σ_{UTS} and the tests were performed until reaching the number of cycles that yielded a 90 % survival probability. To calculate such number of cycles, a statistical approach based on Weibull statistics was applied to predict the failure probability as a function of stress amplitude. Because direct access to damage levels is not easy in fatigue experiments, this approach was necessary to account for the differences in properties between the two systems and enable meaningful comparisons. The main aim of this analysis was to determine the survival probability as a function of the applied stress $F_s(\sigma)$ to ensure that each sample received a similar amount of damage, thereby enabling the determination of the number of cycles for each test. This approach was derived from that described by Hostettler et al. [29], who tested the healability of epoxy-based composite laminates. Through this statistical approach, described also by other authors [30,31] and reported in detail in the Supplementary Materials, the general survival probability curve $F_s(\sigma)$ as a function of the stress was derived as reported in Equation (8),

$$F_s(\sigma) = e^{-\left(\frac{x}{\alpha(\sigma)}\right)^{\beta(\sigma)}}, \tag{8}$$

which can be used to draw survival curves at any stress value comprised between the minimum and maximum stresses applied in the fatigue tests (0.6 ·σ_{UTS} to 0.9 ·σ_{UTS} in this case). The employed Weibull approach was in fact needed to derive the Weibull parameters $\alpha(\sigma)$ (shape factor) and $\beta(\sigma)$ (scale factor) as a function of the applied stress. After calculating the number of cycles yielding a survival probability of 90 % ($N_{90\%}$) at 0.67 σ_{UTS} for the two materials, the specimens were cycled for $N_{90\%}$ cycles, then thermally mended, then cycled again for $N_{90\%}$ cycles, and so on until failure. Thermal mending was performed in an oven at 160 °C for 1 h under no pressure, and then cooling to room temperature. The elastic modulus was measured after each damage and healing step to evaluate the introduced damage and effects of healing. This was performed in the fatigue testing machine by applying a strain of up to 0.3 % at a rate of 1 mm/min. The modulus was measured as the maximum initial slope of the stress-strain curve. No extensometer was used, which could have affected the results, but the obtained values were sufficient to detect any damage or healing. The healing performance was determined by evaluating both the moduli and number of cycles to failure.

3. Results and discussions

3.1. Rheological properties and fiber orientation

Fig. 1a-c illustrates the results of the dynamic rheological measurements on the four samples and shows the trends of η^*, G', and G'' as a function of the angular frequency. The addition of COC and E-GMA increases the complex viscosity, particularly in the low-frequency region. As already observed in our previous work on the optimization of PA6/COC/E-GMA self-healing blends [24], this increase in viscosity occurs because of the high viscosity of COC and the compatibilization promoted by E-GMA. In fact, the epoxide rings of E-GMA chemically react with the amine end groups and/or amide functionalities within the PA6 chains, resulting in the formation of a PA-g-EGMA copolymer at the interfacial area, whereas the ethylene component of E-GMA interacts non-covalently with COC, thereby promoting compatibilization [32,33]. The same effects are responsible for the increase in the storage and loss moduli.

As expected, adding CFs to PA6 also results in a significant increase in η^*, G', and G'', especially at low frequencies. This effect is likely attributed to the rigid nature of the CFs, which impedes the flow of the melt [34]. It is interesting that the increase in viscosity is less evident at higher angular frequencies, which suggests that the prepared blends and composites maintain good processability in high-shear-rate processes such as injection molding.

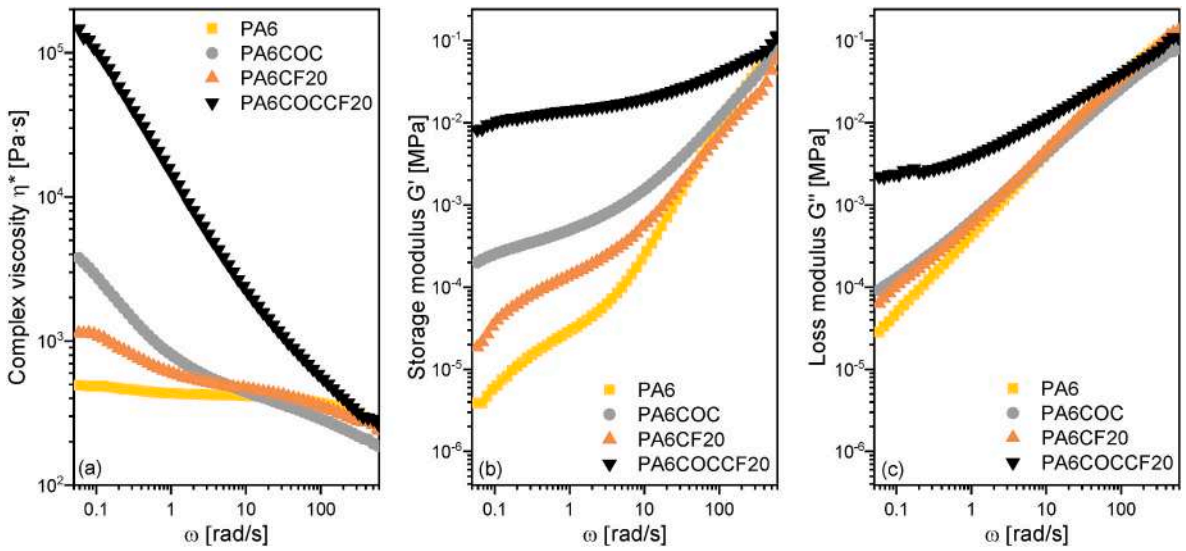

Fig. 1. Results of the dynamic rheological tests at 230 °C. (a) Complex viscosity, (b) storage modulus, and (c) loss modulus as a function of frequency.

The impact of the injection molding process on the microstructure was then assessed using microscopy. Fig. 2a presents optical micrographs of the polished PA6COC blend, which was examined by taking samples from three zones within the narrow parallel portion of the dumbbell specimen. Zone 1 is located near the specimen surface, Zone 2 represents the intermediate region, and Zone 3 corresponds to the specimen's core along its central axis. Near the surface (Zone 1), the combination of low fluid velocity and rapid cooling creates small, spherical COC domains without a specific orientation. This uniformity arises from the rapid solidification process, which constrains COC molecular mobility and prevents directional alignment. As the analysis moves towards the specimen's center, the microstructure evolves significantly. In zone 2, the intermediate region, COC domains become larger and more elongated, aligned with the flow direction. This

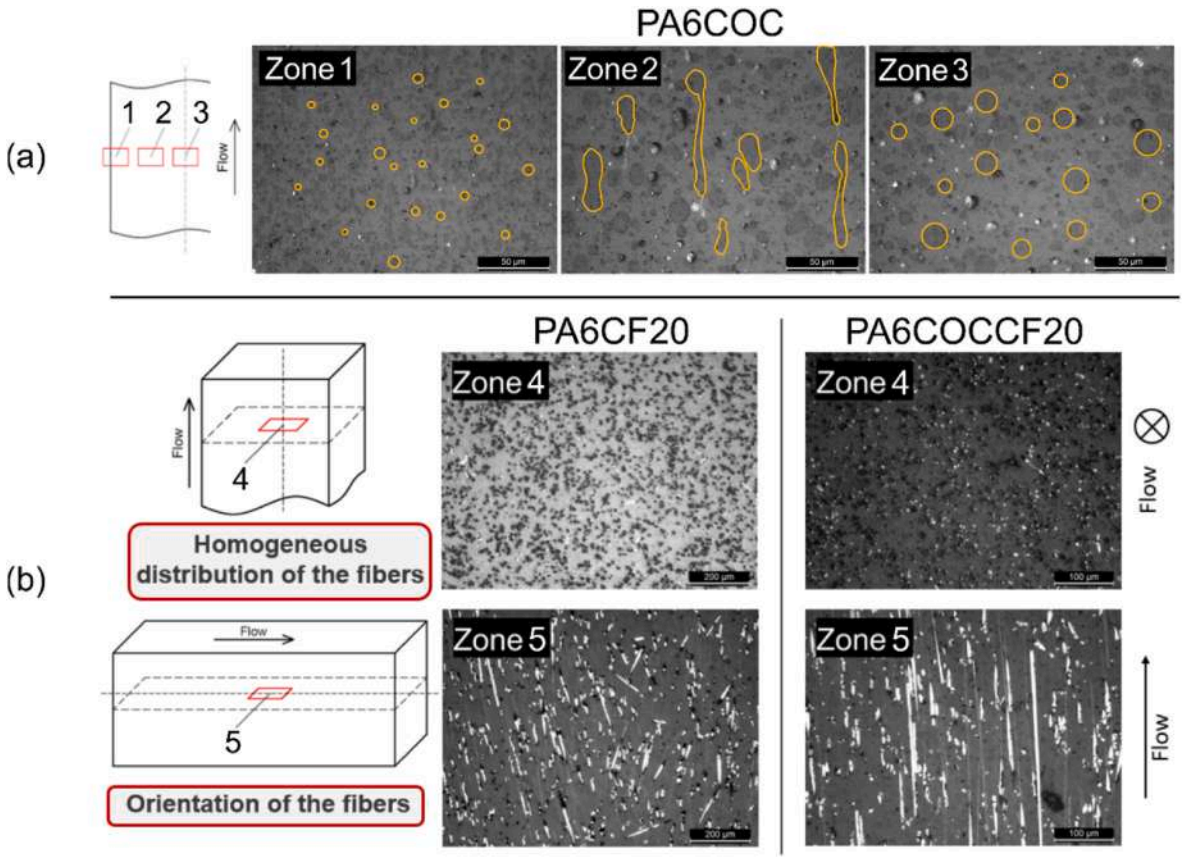

Fig. 2. Light optical micrographs of the prepared samples. (a) Schematic representation of the three different locations where the specimens of PA6COC were taken and micrographs of the polished cross-sections of the corresponding zones. (b) Schematic representation of the location where the specimens of PA6CF20 and PA6COCCF20 were taken and micrographs of the polished cross-sections of the corresponding zones. Arrows represent the direction of material flow during injection molding. White dots are caused by light reflection on the CFs.

transformation results from increased shear forces that stretch the COC droplets during flow, coupled with moderate cooling rates able to fix the domains in the elongated position. The central zone (Zone 3) exhibits distinct microstructural characteristics, featuring predominantly spherical COC domains larger than those observed near the surface. This morphology can be explained by the complex relationship between the flow dynamics and temperature gradient within the cross-section of the specimen. Drawing from Prohm et al.'s work [35], even though the fluid velocity reaches its peak at the center, the velocity gradient remains more uniform in this region, especially at aspect ratios (width/thickness) of 0.25–1.0 (0.4 in this work). This may not favor the elongation of the COC domains. Alternatively, the flow does elongate the COC domains, but the cooling rate is too slow to fix them in the elongated shape. The long permanence at high temperatures causes the COC phase to regain a thermodynamically favorable spherical shape and coalesce.

This second explanation is most likely, given that the flow in the central portion of the specimen is sufficient to align the CFs. This is evident from Fig. 2b, which shows the optical micrographs of the polished surfaces of specimens taken from the center of the composites both across (Zone 4) and along (Zone 5) the flow direction. It is evident that the CFs are well aligned with the direction of the flow and are distributed throughout the entire matrix volume. From a different set of micrographs not reported for the sake of brevity, it is possible to notice that the fibers at the core are more oriented than those near the sides. This is due to the parabolic shape of the fluid velocity gradient, where the highest speed is achieved at the center, promoting fiber alignment, whereas at the edges, the velocity drops to zero, leading to a more random fiber orientation.

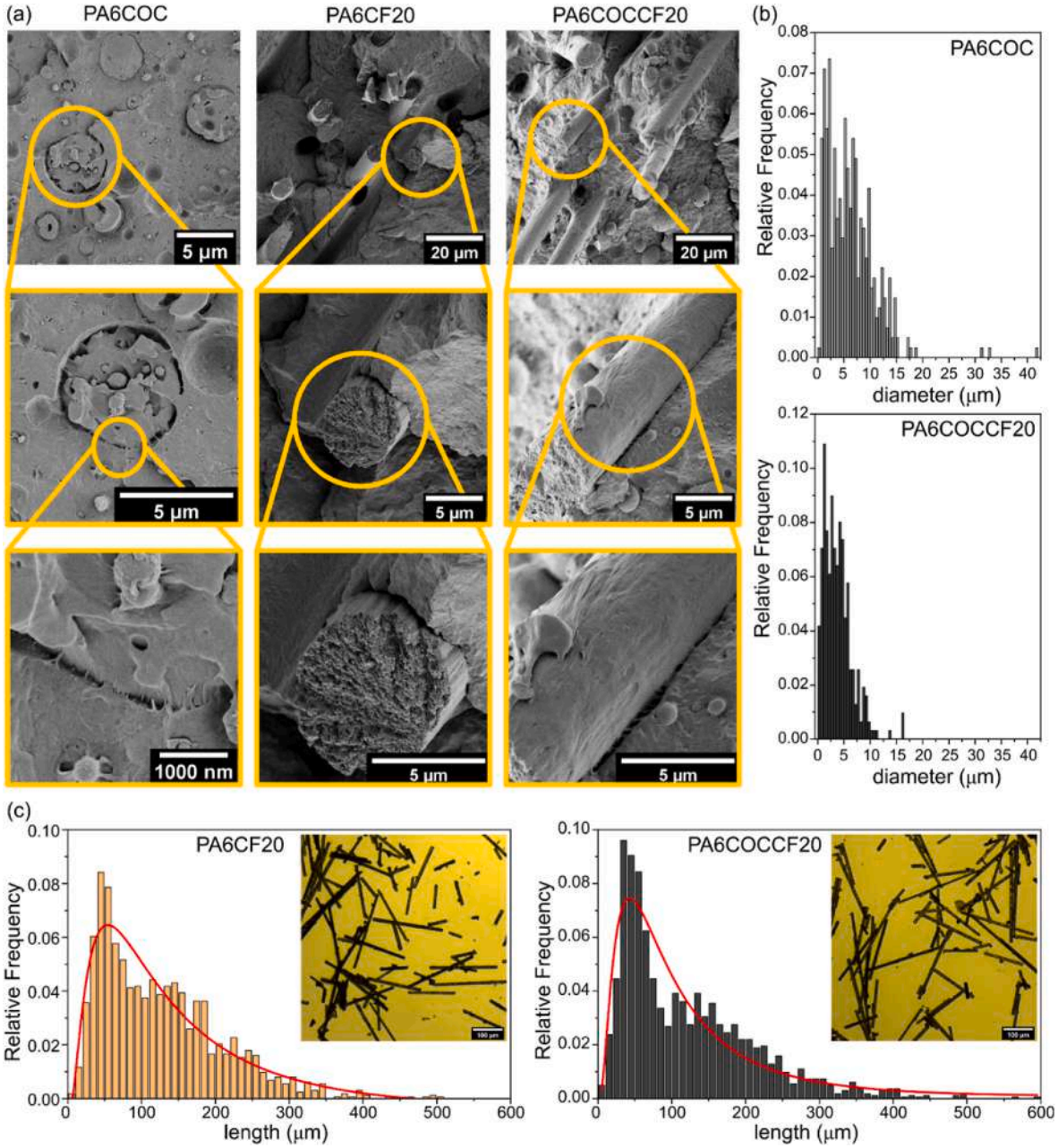

Fig. 3. (a) FESEM micrographs of the cryofractured surfaces of the PA6COC, PA6CF20, and PA6COCCF20 specimens at different magnifications; (b) COC domain size distribution in PA6COC and PA6COCCF20; (c) light optical microscope micrographs of the fibers retrieved from the prepared composites and their relative length distributions.

3.2. Microstructural and thermal properties

Fig. 3a shows FESEM micrographs of the cryofractured surfaces of the PA6COC, PA6CF20, and PA6COCCF20 specimens.

The COC domains show moderate interfacial adhesion with the PA6 matrix, promoted by the E-GMA compatibilizer. This good but not exceptional surface interaction is crucial for the self-healing mechanism, as on one hand it ensures adequate adhesion between the COC and PA6, which is necessary to retain structural integrity and good mechanical properties while preserving the necessary mobility of the COC domains for self-healing purposes. An E-GMA content of 5 wt% is the optimal compatibilizer concentration to achieve this dual goal, as demonstrated in our previous work on the optimization of PA6/COC/E-GMA blends [24]. Fig. 3 also shows FESEM micrographs of the cryofractured surfaces of the PA6CF20 and PA6COCCF20 composites. In PA6CF20, CFs appear to be oriented along the main axis of the specimen, in good agreement with the light microscopy images. The fiber/matrix adhesion is not exceptional despite the polyamide-optimized CF sizing. This is evidenced by severe fiber pull-out and clean lateral fiber surfaces, where crenulation [36] is still appreciable. The fiber/matrix interface seems to be improved in the composite PA6COCCF20. By observing the lateral surfaces of the CFs, the crenulation is no longer visible, which indicates that the pulled-out fibers are covered with a thin matrix film. This may be due to unreacted E-GMA reacting with the fiber sizing, thereby producing a stronger interphase; however, further analysis is needed to fully clarify this aspect.

The FESEM micrographs of the cryofracture surfaces of PA6COC and PA6COCCF20 also allowed the measurement of the average COC domain diameter and size distribution (Fig. 3b). PA6COCCF20 shows slightly smaller COC domains (3.8 ± 2.7 μm) compared to PA6COC (6.2 ± 4.7 μm) and a narrower diameter distribution, probably caused by the presence of the carbon fibers and the higher viscosity of the system, which hindered COC coalescence.

DSC tests (see Supplementary Materials, Fig. S2a, Table S2) reveal very shallow signals at 50–65 °C, associated with the glass transition temperatures of PA6 and COC. The first heating scan shows PA6's characteristic melting at 227.1 °C, indicating stable α-phase crystallization. The introduction of COC slightly impairs PA6 crystallization, as observed in our previous work, and so does the addition of carbon fibers. TGA in nitrogen atmosphere (Fig. S2b, Table S2) demonstrates near-complete decomposition at 700 °C for PA6 and PA6COC (residues 0.8–0.9 wt%), with carbon fiber-reinforced composites maintaining residual masses (20.2-19.9 wt%) consistent with nominal fiber concentrations.

TGA tests also allowed the measurement of the experimental fiber length inside the composites. Fig. 3c shows optical micrographs of the fibers retrieved from the composites and the fiber length distribution. It is evident that the shear stresses during the extrusion and injection molding processes severely shorten the CF. The final fiber length is considerably shorter than the initial fiber length (6 mm). The lognormal mean of the fiber length is 190 μm for PA6CF20 and 127 μm for PA6COCCF20, which may reflect the higher viscosity of the latter. However, the fiber length distribution is quite broad, extending approximately between 1 and 500 μm, with little difference between PA6CF20 and PA6COCCF20 (Table 2). This is similar to that reported by Karsli et al. [27] for PA6/CF composites. They also observed a considerable reduction in fiber length from the initial 6 mm, and reported a length of 50–200 μm after extrusion and injection molding. In the present work, greater preservation of the pristine fiber length could be achieved by modifying the extrusion parameters using several approaches. The first is to modify the extruder design by reducing the mastication elements and ensuring that the fibers are introduced at a point closer to the extruder exit. This approach guarantees a shorter residence time for the fibers inside the extruder. Alternatively, the residence time can be limited by adjusting the processing parameters, such as increasing the flow rate [37–39].

Table 2
Results of the microstructural characterization and composition of the prepared samples.

	PA6	PA6COC	PA6CF20	PA6COCCF20
$w_{f,exp}$ [%]	–	–	20.2	19.9
ρ_{exp} [g/cm^3]	1.070 ± 0.012	1.010 ± 0.011	1.160 ± 0.007	1.093 ± 0.008
ρ_{th} [g/cm^3]	–	–	1.154	1.097
V_v [vol%]	–	–	0.0	0.3
$v_{f,exp}$ [%]	–	–	13.7	13.1
COC domain size [μm]	–	6.2 ± 4.7	–	3.8 ± 2.7
CF length, lognormal mean [μm]			190	127
CF length, mean ± s.d. [μm]	–	–	125 ± 82	120 ± 91

$w_{f,exp}$ = experimental CF weight fraction, measured by TGA; ρ_{exp} = experimental pycnometric density; ρ_{th} = theoretical density; V_v = void volume fraction; $v_{f,exp}$ = experimental fiber volume fraction.

3.3. Mechanical properties

The prepared matrices and composites were then mechanically characterized via tensile, fracture toughness, impact, and fatigue tests. Table 3 reports the results of the quasi-static tensile tests in terms of the average values and standard deviation of E, σ_{UTS}, and ε_b. In terms of the elastic modulus, neat PA6 and PA6COC exhibit nearly the same values. On the other hand, when CFs are incorporated into the matrices, PA6CF20 has an elastic modulus of 13.5 ± 0.3 GPa, while PA6COCCF20 manifests a stiffness of 12.8 ± 0.3 GPa, with an increase of 475 % and 568 % compared to PA6 and PA6COC, respectively. The slightly lower elastic modulus of the self-healing composites is caused by the presence of the healing agent and the compatibilizer. As expected, the mechanical properties of the prepared composites are very high, i.e., PA6CF20 reports σ_{UTS} = 178.2 ± 2.8 MPa and ε_b = 4.3 ± 0.6 %, while PA6COCCF20 reports σ_{UTS} = 143.3 ± 2.0 MPa and ε_b = 5.0 ± 0.3 %. The lower mechanical properties of self-healing composites stem from COC's inherently lower stiffness compared to PA6, the plasticizing effect of E-GMA on PA6, and stress concentration at phase interfaces despite compatibilization. Furthermore, the COC mobility necessary for healing inherently compromises mechanical performance. However, this trade-off is justified by the significant improvements in impact resistance and fatigue life extension provided by the self-healing capability, as detailed in the subsequent sections. Interestingly, the strain at break of the self-healing composite is slightly higher than that of the reference PA6CF20 system, which is probably due to the greater ductility of the self-healing matrix. The experimental results obtained for both PA6CF20 and PA6COCCF20 describe mechanical properties similar to those reported for CF composites with discontinuous aligned fibers [40,41].

The results of the fracture toughness tests (Table 3) show that the introduction of COC dramatically reduces K_{IC} and G_{IC} by more than

Table 3
Results of the mechanical properties of the prepared samples (quasi-static tensile test, quasi-static fracture toughness tests, and Charpy impact tests).

	PA6	PA6COC	PA6CF20	PA6COCCF20
E [GPa]	2.85 ± 0.04	2.26 ± 0.08	13.54 ± 0.30	12.81 ± 0.28
σ_{UTS} [MPa]	67 ± 4	42 ± 1	178 ± 3	143 ± 2
ε_b [%]	5.1 ± 1.3	6.5 ± 0.5	4.3 ± 0.6	5.0 ± 0.3
K_{IC} [MPa·m$^{1/2}$]	3.4 ± 0.5	1.1 ± 0.1	6.0 ± 0.6	5.2 ± 0.5
G_{IC} [kJ/m^2]	6.0 ± 0.6	1.2 ± 0.2	7.6 ± 1.4	6.9 ± 0.9
F_{max} [N]	189 ± 17	112 ± 10	282 ± 23	306 ± 26
$E_{sp,tot}$ [kJ/m^2]	5.2 ± 0.9	2.3 ± 0.3	3.7 ± 0.5	6.3 ± 1.0

three times, as already observed in our previous study on the optimization of PA6/COC/E-GMA blends [24]. On the other hand, the addition of CFs greatly improves the fracture toughness by acting as an obstacle to crack propagation, in good agreement with the results reported in the literature [42,43]. K_{IC} increases by 175 % with a PA6 matrix (PA6CF vs PA6) and, remarkably, of 465 % with a self-healing matrix (PA6COCCF vs PA6COC), likely due to the better fiber/matrix interaction. Hence, the addition of CFs helps increase the fracture toughness of neat PA6 also in the composite with a PA6COC matrix. From the analysis of the load-deflection curves (Fig. S3), it can be noticed that the fracture propagation in PA6 and PA6CF20 samples is brittle, with the crack propagating immediately after the initiation and suddenly leading to failure. On the other hand, in the COC-containing healable systems (PA6COC and PA6COCCF20), although the measured maximum load is lower than that of samples with a neat PA6 matrix, the load does not drop immediately to zero after the maximum, but energy is absorbed also during the crack propagation.

The results of the Charpy impact test (Table 2, Fig. S4) show that neat PA6 exhibits a Charpy impact energy nearly twice as high as that of PA6COC. From visual observation, the fracture surfaces (not reported) of the neat PA6 specimens are irregular and characterized by the detachment of several fragments at the impact zone, denoting the initiation and propagation of various cracks. In contrast, the PA6COC shows a flat fracture surface. The addition of the CFs to neat PA6 causes an increase in F_{max} but a decrease in $E_{sp,tot}$. The reduction in the Charpy impact energy upon the introduction of CF in PA6 was also demonstrated by Dike et al. [44], who attributed this behavior to the formation of concentrated areas at the fiber ends, which favors fiber/fiber interactions, causing a steep decrease in the Charpy impact energy. This has also been observed for other thermoplastic composites reinforced with discontinuous carbon fibers, particularly those with a limited fiber/matrix adhesions [45,46].

In contrast, PA6COCCF20 shows the highest impact force and the highest absorbed energy, which is almost three times higher than that of PA6COC and 170 % higher than that of PA6CF20. The enhanced impact behavior of PA6COCCF20 compared to PA6CF20 is attributed to the increased fiber/matrix interaction owing to the presence of E-GMA [47], which is in good agreement with the SEM observations. Both PA6CF20 and PA6COCCF20 report a very irregular fracture surface, but without the formation of the fragments observed for neat PA6. This ensures optimal contact and adhesion between the two parts during the healing process, thus ensuring a reliable thermal mending process.

3.4. Healing efficiency in fracture toughness and impact conditions

Healing treatment was performed on all the prepared composites, but only those containing COC had sufficient mechanical integrity to be handled and retested after healing, while the samples PA6 and PA6CF broke into two pieces immediately after removal from the oven. Hence, the healing efficiency of these two samples was practically close to zero.

Fig. 4 shows the healing efficiency of the COC-containing samples obtained from fracture toughness tests and Charpy impact tests in three subsequent testing/healing cycles. As expected, the *HE* values obtained from the quasi-static fracture toughness tests are limited (max. 10 % for PA6COC), as observed in our previous work [24]. Due to the severe plasticization of PA6, the COC is trapped inside the dimples caused by the plasticization and is therefore unable to fill the crack plane during thermal mending. This situation is further complicated by the CFs (HE max 2.9 % for PA6COCCF20), which further hinder the COC flow. However, the results are reliable, because the HE values are consistent across the three healing cycles.

In contrast, the *HE* results obtained from the Charpy impact tests are considerably higher (max. 80 % for PA6COC and 51 % for PA6COCCF20), demonstrating the substantial capability of the matrix to restore a significant portion of its mechanical properties.

The lower *HE* values observed for the PA6COCCF20 composite in both tests can be attributed to two factors. First, during the impact tests, the fibers situated within the crack plane may experience breakage, and this damage does not heal during thermal mending, which makes the fibers in the crack zone unable to contribute mechanically to the properties of the healed specimens. Second, the morphology of the crack plane is even more irregular than that of the matrices. Consequently, the softened COC is unable to adequately infiltrate and fill the crack plane, resulting in suboptimal healing. Despite these limitations, the results remain promising and display high efficiency even after the third cycle, demonstrating the repeatability of the healing process in the same zone.

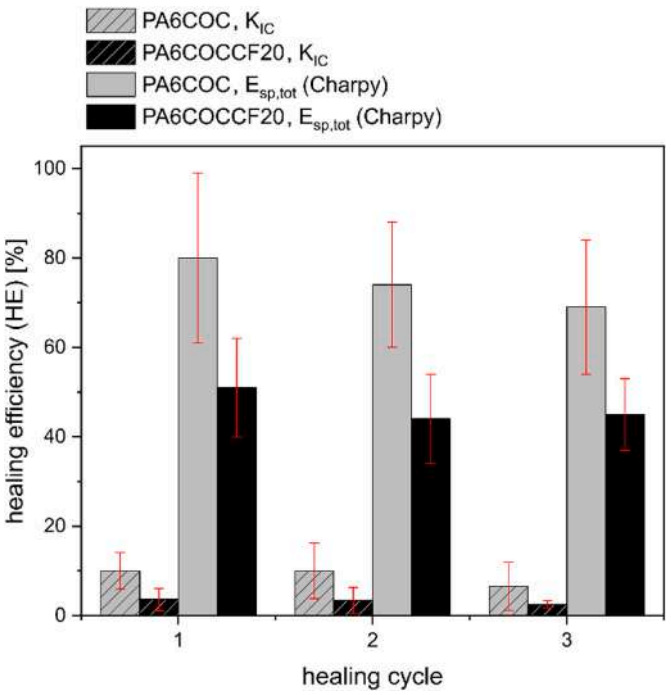

Fig. 4. Healing efficiency calculated on PA6COC (gray) and PA6COCCF20 (black) considering the values of the fracture toughness (K_{IC}, dashed) and total Charpy impact energy ($E_{sp,tot}$, solid).

The lack of mobility experienced by COC in the crack zone can be better appreciated by looking at Fig. 5, which shows the FESEM micrographs of the fractured PA6COC and PA6COCCCF20 specimens tested in the quasi-static fracture toughness and Charpy impact tests after each healing cycle. In the PA6COC sample, in quasi-static mode, the motion of the COC is severely hindered by the presence of the plasticized matrix. As a result, COC is able to flow and cover the crack plane only to some extent. However, in the impact mode, the fracture surface is more planar and the PA6 phase is less plasticized, which allows the COC to flow without any obstacles. Thus, a thin and homogeneous layer of softened COC is observable on the crack plane for all the three healing cycles.

In the PA6COCOCF20 composite, the fractured surfaces of the specimens tested in quasi-static mode are also severely plasticized and made even more irregular by the presence of CF, which confines the softened COC in specific locations. Thus, COC is only partially able to fill the crack plane, which explains the limited *HE* values. On the other hand, in impact mode, the fracture surfaces are much more planar, and the COC can flow across longer distances. These findings underscore the importance of developing strategies to promote infiltration of healing agents. In conclusion, while the PA6COCCF20 composite demonstrates a significant healing capacity, the observed limitations point to areas for further investigation and improvement.

The differences in the healing capacity between the unreinforced and reinforced specimens also indicate another critical aspect. Once the reinforcing fibers are damaged, it is impossible to achieve high healing

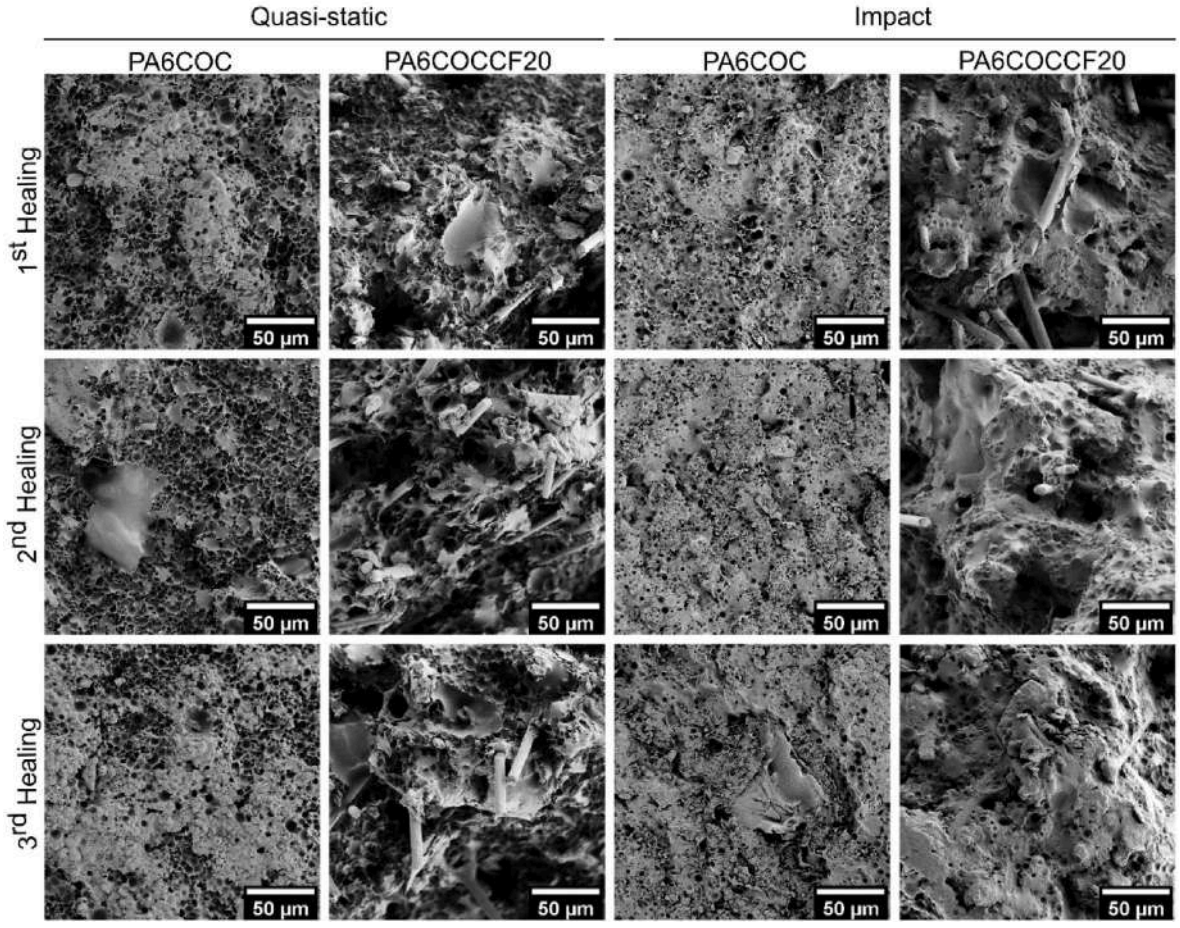

Fig. 5. FESEM micrographs of the PA6COC and PA6COCCF20 specimens tested in quasi-static fracture toughness and Charpy impact tests, after the thermal mending process.

efficiency values because the healing process does not repair broken fibers and, in most cases, not even broken interfaces. Hence, advancements in the field of self-healing matrices must be coupled with progress in techniques for early detection and healing of matrix-related microdamage. This work contributes to this aspect by studying the thermal healing of a composite when microdamage is introduced by fatigue testing, which is also closer to real case scenarios. The results of this approach are presented in the next section.

3.5. Fatigue tests and healing of the fatigue microdamages

The prepared composites, PA6CF20 and PA6COCCF20, were tested under fatigue conditions, and the obtained Wöhler curves are shown in Fig. 6a. When the two composites are compared at the same stress level, PA6CF appears to outperform PA6COCCF20 under fatigue conditions, exhibiting a higher number of cycles to failure at any given stress level. However, this occurs because PA6CF exhibits a higher tensile strength, and in fact when each Wöhler curve is normalized to the corresponding

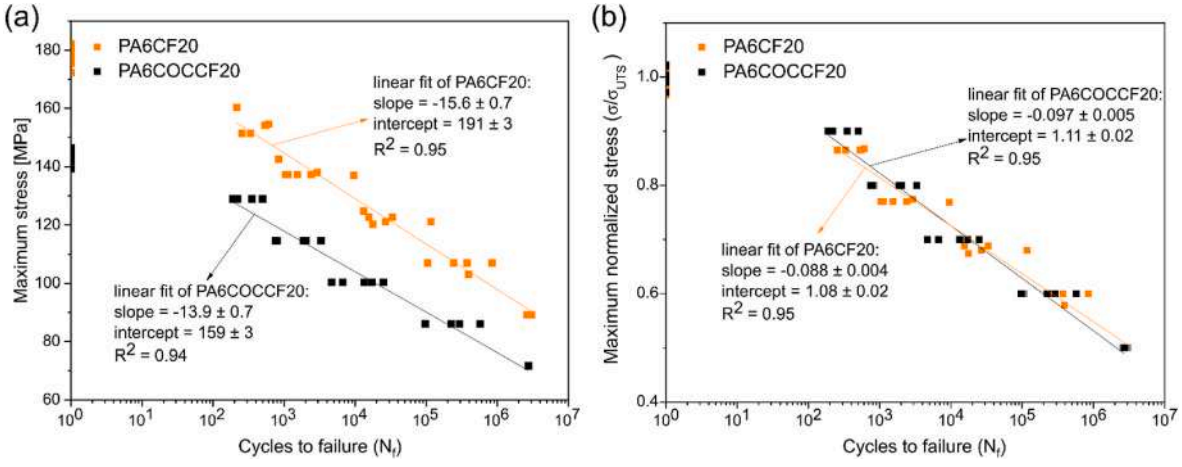

Fig. 6. Wöhler curves of PA6CF20 and PA6COCCF20 composites. Maximum stress (a) and normalized maximum stress (b) as functions of number of cycles to failure.

σ_{UTS} (Fig. 6b), it is evident that the two materials exhibit a very similar fatigue behavior. Hence, the presence of the healing agent does not seem to improve the fatigue life of the composite, unlike what has been observed in the literature for other self-healing composites, for example by Hostettler et al. [29], Pingkarawat et al. [20–22], and Ladani et al. [23]. However, in these cases, the matrix was a brittle epoxy resin, and the authors attributed the improvement in the fatigue behavior and the retardation of the fatigue crack growth to an increase in the matrix toughness owing to the presence of the thermoplastic healing agent. Nevertheless, in the present study, the fatigue behavior is not worsened by COC.

The real improvement of the healable system developed in this work emerges when considering the remarkably different capacities of the two systems for repairing fatigue-related microdamage. The statistical approach based on Weibull statistics was applied to predict the failure probability of the samples as a function of the applied stress amplitude (see Supplementary Materials, Fig. S1, Table S1). This approach was used to determine the stress amplitude and number of cycles necessary to reach a similar extent of damage in PA6CF20 and PA6COCCF20 before healing and retesting to assess whether the fatigue life was enhanced. This was necessary because the two materials have different tensile and fatigue performances, and simply selecting the same stress level and number of cycles would damage the two materials differently.

This approach resulted in the survival probability curves reported in Fig. 7a,b, where the continuous curves represent are those obtained from the experimental data and the three dotted curves are obtained from the model, imposing a desired load level. Now, the number of cycles related to 90 % of the survival probability ($N_{90\%}$) can be extrapolated for any given stress amplitude. In this case, the selected stress level is 0.67 σ_{UTS}, corresponding to 120 MPa for PA6CF20 and 95 MPa for PA6COCCF20, resulting in 27569 and 28574 cycles, respectively, indicated by the arrows in Fig. 7a,b. These specific stress and failure probability values were chosen to perform a test of approximately 3 h to simulate a realistic working scenario for the material and to introduce a certain amount of microdamage. Increasing the applied stress would have resulted in a lower number of cycles, which would have increased the uncertainty and promoted premature failure due to possible microstructural defects in the tested specimens, and decreasing the applied stress would have excessively increased the testing time for each specimen.

Fig. 8a shows the Wöhler curves of the virgin specimens and the data points of the specimens subjected to the damaging/healing procedure. As expected, the PA6CF20 specimens cannot heal, and thus break in the vicinity of the predicted range. The inability of PA6CF to heal is also evident from the trends in the elastic modulus of the virgin, damaged, and healed specimens, as shown in Fig. 8b. If the first damage step impairs the stiffness of the material, it does not recover at all during healing. In fact, none of the tested samples survived the second fatigue damage step.

Conversely, the PA6COCCF20 specimens can sustain more damaging/healing cycles and exceed the predicted fatigue life at the testing stress amplitude. The experimental points of the healed specimens (red squares, Fig. 8a) are shifted to the right with respect to the linear fitting of the virgin specimens (black squares). The recovery of mechanical integrity is also evident from the trends in the elastic moduli (Fig. 8b). As expected, for all specimens, cyclic loading causes a reduction in the elastic modulus, indicating microdamage accumulation. The healing process instead allows a certain recovery of the elastic modulus, which is evident after the first and second healing cycles. However, the stiffness recovery is incomplete, and the healing process performs worse after the second cycle than after the first. Moreover, the data scattering also increases as the test progresses, which may also be associated with the accumulation of damage inside the material. Nevertheless, after the damaging/healing processes, by comparing the averages of N_f of the healed and virgin samples (reported on the Wöhler curves in Fig. 8a), the healing process extends the fatigue life of the healable PA6COCCF20 composite by 76.9 %.

To dig deeper in the mechanism involved in the fatigue life extension of PA6COCCF20, FESEM micrographs of the damaged/healed specimens are reported in Fig. 8c. The micrographs are taken from the stable crack propagation zone, i.e., in the zone where progressive damage accumulates. In the micrographs of PA6COCCF20, a thin and homogeneous layer of COC is present on the surface of the crack plane, which makes the fracture surface quite different from that of PA6CF20. During the damage process, several microcracks are formed, and upon thermal mending, the COC softens and can flow and fill them, which explains the partial recovery of the elastic modulus and the extended fatigue life of the self-healing composites. However, the COC flow may be partially hindered by the extended plasticization observed in the stable crack propagation zone [24]. This effect is not observed in epoxy matrices, which instead show a plain fracture surface, and may explain the higher *HE* generally observed in epoxy composites [20–23].

The self-healing mechanism in PA6COCCF20 follows distinct stages during thermal treatment. At 160 °C, COC domains ($T_g \sim 65$ °C) selectively soften while PA6 ($T_m \sim 220$ °C) maintains structural stability. Capillary forces drive softened COC into fatigue-induced microcracks, followed by resolidification upon cooling, creating physical bridges across damaged regions. This process depends on COC domain proximity to cracks, damage site accessibility, crack morphology, and the healing temperature-time profile. Fatigue damage is particularly

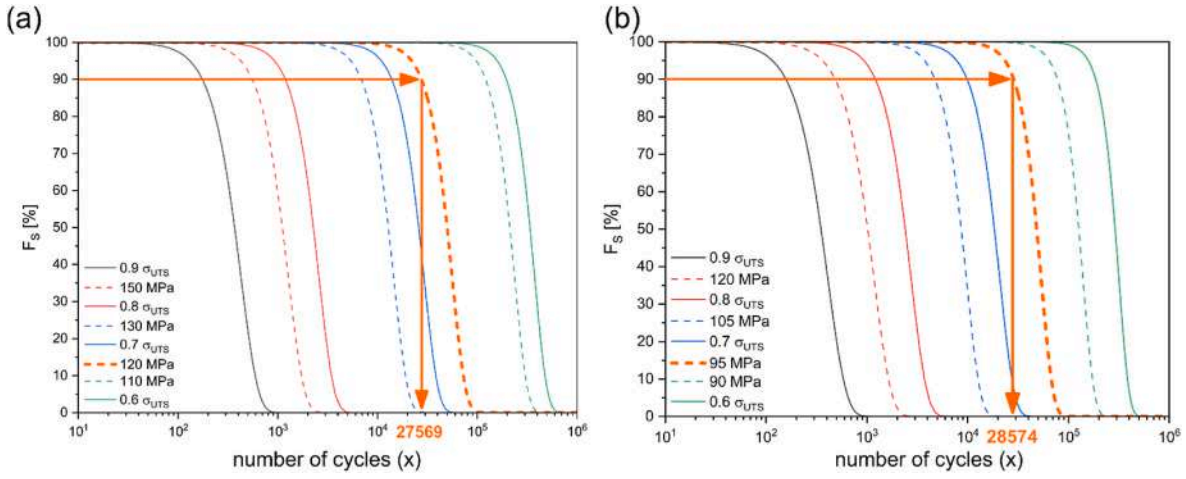

Fig. 7. Survival probability curves with the indication of the cycles at 90 % survival probability for a stress level of 0.67 σ_{UTS} for (a) PA6CF20 and (b) PA6COCCF20 composites.

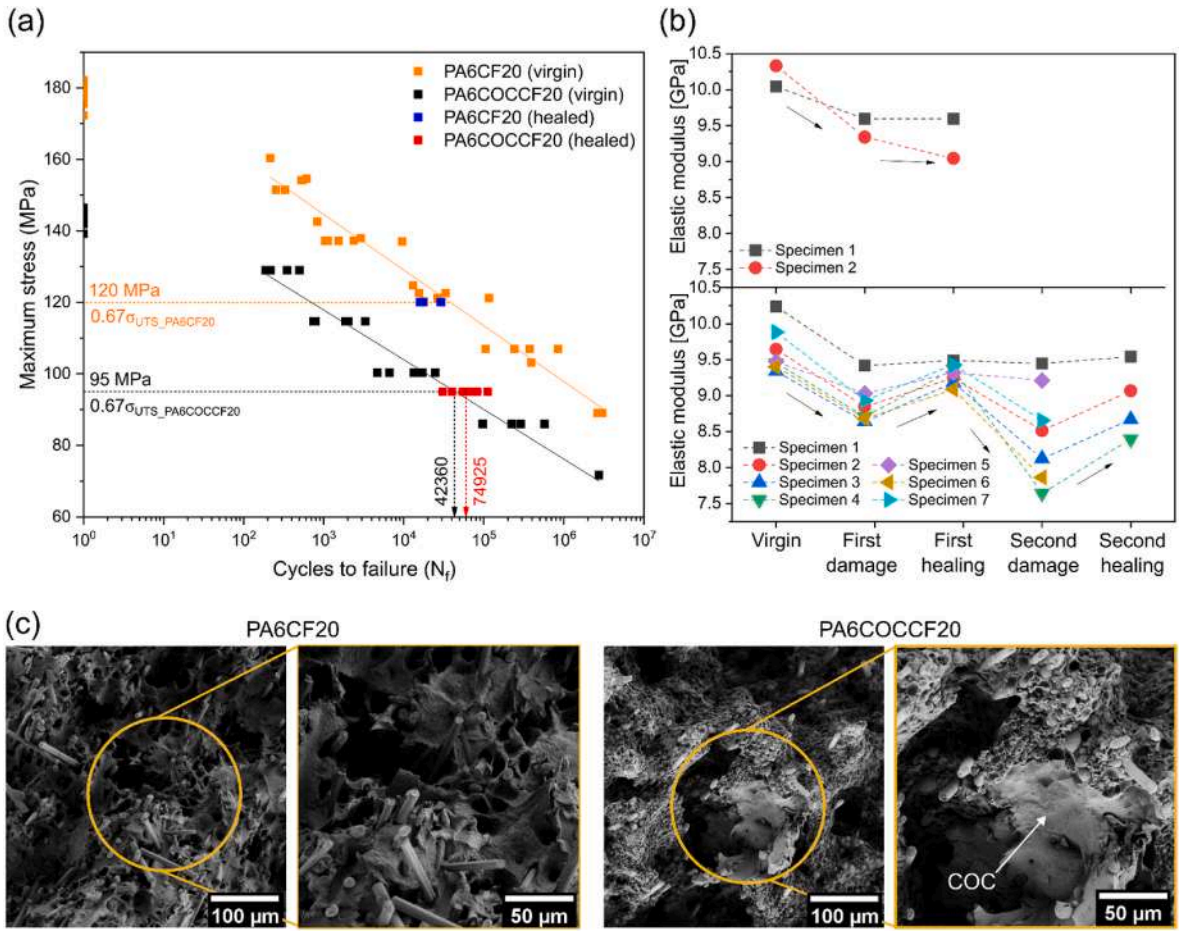

Fig. 8. (a) Wöhler curves, linear fitting, and cycles to failure of the damaged/healed specimens of PA6CF20 and PA6COCCF20; (b) variation in the elastic modulus throughout the damage/healing process of two PA6CF20 specimens (top) and seven PA6COCCF20 specimens (bottom); (c) fracture surfaces of PA6CF20 and PA6COCCF20 samples after fatigue damaging/healing.

suitable to be healed via this healing mechanism as it creates networks of matrix microcracks before catastrophic fiber failure, explaining the higher healing efficiency in fatigue applications compared to repairing macroscopically fractured samples.

Hence, this study highlights the critical aspects that influence the healing efficiency of polymer composites, particularly the role of fiber integrity and crack plane morphology. These findings highlight the importance of developing strategies to enhance the infiltration capability of healing agents to enhance the structural integrity of composites during repeated healing cycles. Future research could focus on further optimizing the composition and properties of the healing agents to better penetrate and fill irregular crack planes, thereby enhancing the overall healing efficiency.

4. Conclusions

The conclusions drawn from this comprehensive study highlight the significant impact of incorporating COC as a healing agent and E-GMA as a compatibilizer into PA6 matrices, particularly when reinforced with carbon fibers. While the addition of COC and E-GMA slightly reduced the mechanical properties of the PA6 matrix, the incorporation of carbon fibers significantly enhanced the stiffness and strength of both neat PA6 and the self-healing PA6/COC/E-GMA blend. Although the self-healing blend showed a lower fracture toughness than neat PA6, the addition of carbon fibers greatly improved the fracture toughness of both systems. Notably, in the impact tests, the self-healing composite (PA6COCCF20) demonstrated the highest impact force and absorbed energy among all the tested materials.

The healing efficiency of the system varied depending on the test conditions. In fracture toughness tests, the efficiency was limited due to matrix plasticization and CF presence hindering COC flow. However, higher healing efficiencies were achieved in impact tests, particularly for the unfilled blend. Fatigue tests revealed similar normalized fatigue behaviors for both the reference and self-healing composites, with the self-healing composite demonstrating a remarkable ability to repair fatigue-induced microdamage.

One of the most significant findings is that PA6COCCF20 is able to extend its own fatigue life by 77 % thanks to thermal mending, while the neat composite PA6CF20 is not able to heal, highlighting the potential of the healable system for applications under cyclic loads. FESEM analysis provides insight into the healing mechanism, showing that during thermal mending, COC flows and fills microcracks formed during fatigue loading, explaining the partial recovery of the elastic modulus and extended fatigue life in the self-healing composite. These results demonstrate the potential of intrinsic self-healing thermoplastic composites based on PA6/COC/E-GMA blends reinforced with carbon fibers, particularly for repairing fatigue-induced microdamage. However, there is still room for improvement in healing efficiency, particularly in addressing fiber damage and enhancing healing agent infiltration in complex crack geometries. Future research should focus on optimizing the composition and properties of healing agents to better penetrate irregular crack planes and further enhance the overall performance of these self-healing composites.

CRediT authorship contribution statement

M. Coser: Writing – review & editing, Methodology, Investigation, Formal analysis, Data curation, Conceptualization. **D. Perin:** Writing – original draft, Validation, Investigation, Formal analysis, Data curation, Conceptualization. **G. Fredi:** Writing – review & editing, Writing – original draft, Visualization, Validation. **L. Aliotta:** Writing – review & editing, Investigation. **V. Gigante:** Writing – review & editing, Investigation. **A. Lazzeri:** Resources. **A. Dorigato:** Writing – review & editing, Supervision, Funding acquisition, Conceptualization. **A. Pegoretti:** Writing – review & editing, Supervision, Project administration, Funding acquisition, Conceptualization.

Funding

Funded by the European Union - Next Generation EU - PNRR, Mission 4 Component 2, Investment 1.3 - PE MICS Spoke 5 - LOLIMAR Project (PE00000004, CUP D43C22003120001).

Declaration of competing interest

The authors declare the following financial interests/personal relationships which may be considered as potential competing interests: Andrea Dorigato reports financial support was provided by European Union. If there are other authors, they declare that they have no known competing financial interests or personal relationships that could have appeared to influence the work reported in this paper.

Appendix A. Supplementary data

Supplementary data to this article can be found online at https://doi.org/10.1016/j.compscitech.2025.111213.

Data availability

Data will be made available on request.

References

[1] M.O.H. Cioffi, A.S.C. Bomfim, V. Ambrogi, S.G. Advani, A review on self-healing polymers and polymer composites for structural applications, Polym. Compos. 43 (11) (2022) 7643–7668, https://doi.org/10.1002/pc.26887.
[2] Z.P. Zhang, M.Z. Rong, M.Q. Zhang, Self-healable functional polymers and polymer-based composites, Prog. Polym. Sci. 144 (2023), https://doi.org/10.1016/j.progpolymsci.2023.101724.
[3] H. Jamil, M. Faizan, M. Adeel, T. Jesionowski, G. Boczkaj, A. Balciunaite, Recent advances in polymer nanocomposites: unveiling the frontier of shape memory and self-healing properties-A comprehensive review, Molecules 29 (6) (2024), https://doi.org/10.3390/molecules29061267.
[4] S. Utrera-Barrios, R. Verdejo, M.A. López-Manchado, M. Hernández Santana, Evolution of self-healing elastomers, from extrinsic to combined intrinsic mechanisms: a review, Mater. Horiz. 7 (11) (2020) 2882–2902, https://doi.org/10.1039/D0MH00535E.
[5] R. Malekkhouyan, R.E. Neisiany, S.N. Khorasani, O. Das, F. Berto, S. Ramakrishna, The influence of size and healing content on the performance of extrinsic self-healing coatings, J. Appl. Polym. Sci. 138 (10) (2021) 49964, https://doi.org/10.1002/app.49964.
[6] J. Wang, J. Tang, D. Chen, S. Xing, X. Liu, J. Hao, Intrinsic and extrinsic self-healing fiber-reinforced polymer composites: a review, Polym. Compos. 44 (10) (2023) 6304–6323, https://doi.org/10.1002/pc.27623.
[7] P.C. Je, M.T.H. Sultan, C.P. Selvan, S. Irulappasamy, F. Mustapha, A.A. Basri, S.N. A. Safri, Manufacturing challenges in self-healing technology for polymer composites — a review, J. Mater. Res. Technol. 9 (4) (2020) 7370–7379, https://doi.org/10.1016/j.jmrt.2020.04.082.
[8] R.J. Varley, D.A. Craze, A.P. Mouritz, C.H. Wang, Thermoplastic healing in epoxy networks: exploring performance and mechanism of alternative healing agents, Macromol. Mater. Eng. 298 (11) (2013) 1232–1242, https://doi.org/10.1002/mame.201200394.
[9] A.R. Jones, C.A. Watkins, S.R. White, N.R. Sottos, Self-healing thermoplastic-toughened epoxy, Polymer 74 (2015) 254–261, https://doi.org/10.1016/j.polymer.2015.07.028.
[10] A.N. Aina, M.A.M. Rizal, M.F.A. Rased, S.A. Hassan, L.F. Ng, L. Rajeshkumar, R. A. Ilyas, H.A. Israr, Fiber-reinforced thermoplastic composites for future use in aircraft radomes: biomimetic design approaches and its performances, Fibers Polym. 25 (12) (2024) 4503–4527, https://doi.org/10.1007/s12221-024-00776-1.
[11] M. Valentini, O. De Almeida, M. Kakkonen, G. Kalinka, A. Dorigato, P. Kallio, G. Fredi, Effect of fiber surface state on the thermomechanical and interfacial properties of in situ polymerized polyamide 6/basalt fiber composites, Composites Part A 190 (2025) 108681, https://doi.org/10.1016/j.compositesa.2024.108681.
[12] A. Pegoretti, Towards sustainable structural composites: a review on the recycling of continuous-fiber-reinforced thermoplastics, Advanced Industrial and Engineering Polymer Research 4 (2) (2021) 105–115, https://doi.org/10.1016/j.aiepr.2021.03.001.
[13] D. Perin, A. Dorigato, A. Pegoretti, Thermoplastic self-healing polymer blends for structural composites: development of polyamide 6 and cyclic olefinic copolymer blends, J. Appl. Polym. Sci. 140 (16) (2023) e53751, https://doi.org/10.1002/app.53751.
[14] D. Perin, G. Odorizzi, A. Dorigato, A. Pegoretti, Development of polyamide 6 (PA6)/Polycaprolactone (PCL) thermoplastic self-healing polymer blends for multifunctional structural composites, Appl. Sci. 12 (23) (2022) 12357, https://doi.org/10.3390/app122312357.
[15] D. Perin, A. Dorigato, A. Pegoretti, Compatibilization of polyamide 6/cyclic olefinic copolymer blends for the development of multifunctional thermoplastic composites with self-healing capability, Materials 17 (8) (2024) 1880.
[16] E. Tsangouri, D. Aggelis, D. Van Hemelrijck, Quantifying thermoset polymers healing efficiency: a systematic review of mechanical testing, Prog. Polym. Sci. 49–50 (2015) 154–174, https://doi.org/10.1016/j.progpolymsci.2015.06.002.
[17] S.Y. Kim, N.R. Sottos, S.R. White, Self-healing of fatigue damage in cross-ply glass/epoxy laminates, Compos. Sci. Technol. 175 (2019) 122–127, https://doi.org/10.1016/j.compscitech.2019.03.016.
[18] A.S. Jones, H. Dutta, Fatigue life modeling of self-healing polymer systems, Mech. Mater. 42 (4) (2010) 481–490, https://doi.org/10.1016/j.mechmat.2010.02.002.
[19] N.J. Vishe, S.B. Mulani, S. Roy, Repeatable self-healing of composite's fatigue delamination, Compos. Struct. 311 (2023) 116846, https://doi.org/10.1016/j.compstruct.2023.116846.
[20] K. Pingkarawat, C. Wang, R. Varley, A. Mouritz, Self-healing of delamination fatigue cracks in carbon fibre–epoxy laminate using mendable thermoplastic, J. Mater. Sci. 47 (2012) 4449–4456.
[21] K. Pingkarawat, T. Bhat, D.A. Craze, C.H. Wang, R.J. Varley, A.P. Mouritz, Healing of carbon fibre–epoxy composites using thermoplastic additives, Polym. Chem. 4 (18) (2013) 5007–5015, https://doi.org/10.1039/C3PY00459G.
[22] K. Pingkarawat, C.H. Wang, R.J. Varley, A.P. Mouritz, Healing of fatigue delamination cracks in carbon–epoxy composite using mendable polymer stitching, J. Intell. Mater. Syst. Struct. 25 (1) (2014) 75–86, https://doi.org/10.1177/1045389x13505005.
[23] R.B. Ladani, C.H. Wang, A.P. Mouritz, Delamination fatigue resistant three-dimensional textile self-healing composites, Compos. Appl. Sci. Manuf. 127 (2019) 105626, https://doi.org/10.1016/j.compositesa.2019.105626.
[24] D. Perin, D. Rigotti, L. Botta, A. Dorigato, G. Fredi, A. Pegoretti, Tuning the compatibilizer content and healing temperature in thermally mendable polyamide 6/cyclic olefin copolymer blends, Polymers 17 (2025) 280, https://doi.org/10.3390/polym17030280.
[25] Q.-X. Liu, Y.-Y. Zhang, Z. Sun, Y.-Q. Li, B.-W. Guan, T. Guan, Y.-T. Fu, X.-L. Mo, S.-Y. Fu, High mechanical performance short carbon fiber reinforced polyetherimide composites via solution mixing process, Compos. Sci. Technol. 244 (2023) 110296, https://doi.org/10.1016/j.compscitech.2023.110296.
[26] C. Millot, L.-A. Fillot, O. Lame, P. Sotta, R. Seguela, Assessment of polyamide-6 crystallinity by DSC, J. Therm. Anal. Calorim. 122 (1) (2015) 307–314, https://doi.org/10.1007/s10973-015-4670-5.
[27] N.G. Karsli, A. Aytac, Tensile and thermomechanical properties of short carbon fiber reinforced polyamide 6 composites, Compos. B Eng. 51 (2013) 270–275, https://doi.org/10.1016/j.compositesb.2013.03.023.
[28] A. Cohades, C. Branfoot, S. Rae, I. Bond, V. Michaud, Progress in self-healing fiber-reinforced polymer composites, Adv. Mater. Interfac. 5 (17) (2018) 1800177, https://doi.org/10.1002/admi.201800177.
[29] N. Hostettler, A. Cohades, V. Michaud, Statistical fatigue investigation and failure prediction of a healable composite system, Frontiers in Materials 7 (2020), https://doi.org/10.3389/fmats.2020.561852.
[30] R. Sakin, İ. Ay, Statistical analysis of bending fatigue life data using Weibull distribution in glass-fiber reinforced polyester composites, Mater. Des. 29 (6) (2008) 1170–1181, https://doi.org/10.1016/j.matdes.2007.05.005.
[31] N.H. Tai, C.C.M. Ma, J.M. Lin, G.Y. Wu, Effects of thickness on the fatigue-behavior of quasi-isotropic carbon/epoxy composites before and after low energy impacts, Compos. Sci. Technol. 59 (1999) 1753–1762.
[32] M. Mehrabi Mazidi, M.K. Razavi Aghjeh, Effects of blend composition and compatibilization on the melt rheology and phase morphology of binary and ternary PP/PA6/EPDM blends, Polym. Bull. 72 (8) (2015) 1975–2000, https://doi.org/10.1007/s00289-015-1384-6.
[33] C. Jiang, S. Filippi, P. Magagnini, Reactive compatibilizer precursors for LDPE/PA6 blends. II: maleic anhydride grafted polyethylenes, Polymer 44 (8) (2003) 2411–2422, https://doi.org/10.1016/S0032-3861(03)00133-2.
[34] X. Li, J. He, Z. Hu, X. Ye, S. Wang, Y. Zhao, B. Wang, Y. Ou, J. Zhang, High strength carbon-fiber reinforced polyamide 6 composites additively manufactured by screw-based extrusion, Compos. Sci. Technol. 229 (2022) 109707, https://doi.org/10.1016/j.compscitech.2022.109707.
[35] C. Prohm, H. Stark, Feedback control of inertial microfluidics using axial control forces, Lab Chip 14 (12) (2014) 2115–2123, https://doi.org/10.1039/C4LC00145A.

[36] J. Wang, D.B. Anthony, C.A. Fuentes, H.G. De Luca, D. Zhang, A. Bismarck, A. W. Van Vuure, M.S.P. Shaffer, D. Seveno, Wettability of carbon nanotube-grafted carbon fibers and their interfacial properties in polypropylene thermoplastic composite, Compos. Appl. Sci. Manuf. 159 (2022) 106993, https://doi.org/10.1016/j.compositesa.2022.106993.

[37] V. Gigante, F. Cartoni, B.D. Pont, L. Aliotta, Extrusion parameters optimization and mechanical properties of bio-polyamide 11-based biocomposites reinforced with short basalt fibers, Genes 16 (2024) 3092, https://doi.org/10.3390/polym16213092.

[38] V. Gigante, G. Gallone, L. Aliotta, A. Lazzeri, Twin-screw extrusion optimization and study of morphological, thermal, mechanical and fracture properties of sustainable Poly(lactic acid) (PLA) and Poly(butylene sebacate) (PBSe) blends, Mater. Today Sustain. 28 (2024) 100953, https://doi.org/10.1016/j.mtsust.2024.100953.

[39] H. Malatyali, V. Schöppner, N. Rabeneck, F. Hanselle, L. Austermeier, D. Karch, A model for the carbon fiber breakage along the twin-screw extruder, SPE Polymers 2 (2) (2021) 145–152, https://doi.org/10.1002/pls2.10040.

[40] A. Hendlmeier, Ž. Simon, A. Chutani, L.C. Henderson, Generating short carbon fiber polyamide-6 composites from continuous carbon fiber – a preliminary examination of surface treatment and sizing effects, Compos. Appl. Sci. Manuf. 138 (2020) 106058, https://doi.org/10.1016/j.compositesa.2020.106058.

[41] L. Quagliato, J. Lee, J.H. Fonseca, D. Han, H. Lee, N. Kim, Influences of stress triaxiality and local fiber orientation on the failure strain for injection-molded carbon fiber reinforced polyamide-6, Eng. Fract. Mech. 250 (2021) 107784, https://doi.org/10.1016/j.engfracmech.2021.107784.

[42] S. Molnár, S. Rosenberger, J. Gulyás, B. Pukánszky, Structure and impact resistance of short carbon fiber reinforced polyamide 6 composites, J. Macromol. Sci. B 38 (5–6) (2006) 721–735, https://doi.org/10.1080/00222349908248134.

[43] J. Shi, X. Zong, W. Jiang, R. Yao, J. Zheng, Evaluation of the fracture toughness of short carbon fiber reinforced thermoplastic composites, J. Eng. Mater. Technol. 146 (2) (2024), https://doi.org/10.1115/1.4063667.

[44] A.S. Dike, Improvement of mechanical and physical properties of carbon fiber-reinforced polyamide composites by applying different surface coatings for short carbon fiber, J. Thermoplast. Compos. Mater. 33 (4) (2020) 541–553, https://doi.org/10.1177/0892705719877218.

[45] D.M. Laura, H. Keskkula, J.W. Barlow, D.R. Paul, Effect of glass fiber and maleated ethylene–propylene rubber content on tensile and impact properties of Nylon 6, Polymer 41 (2000) 7165–7174.

[46] S.-Y. Fu, B. Lauke, Fracture resistance of unfilled and calciteparticle-filled ABS composites reinforced by short glass fibers (SGF) under impact load, Composites Part A 29A (1998) 631–641.

[47] J. Zhang, W. Dong, X. Li, Y. Wei, Z. Hu, E. Shiju, J. Zheng, H. Chen, S. Wang, Optimal short carbon fiber-reinforced polyamide 6 composites with lifted high strength and toughness for fused filament fabrication, Polym. Compos. 45 (16) (2024) 14580–14594, https://doi.org/10.1002/pc.28783.